Applied Physics Reviews ARTICLE pubs.aip.org/aip/are

3D printing of bio-inspired porous polymeric solar steam generators for efficient and sustainable desalination

Cite as: Appl. Phys. Rev. **11**, 031407 (2024); doi: 10.1063/5.0200505
Submitted: 27 January 2024 · Accepted: 3 June 2024 ·
Published Online: 23 July 2024

View Online Export Citation CrossMark

Yanbei Hou,[1,2] Ming Gao,[1,2] Xueyu Bai,[2] Lihua Zhao,[1,3] Hejun Du,[1,2] and Kun Zhou[1,2,a)]

AFFILIATIONS

[1]HP-NTU Digital Manufacturing Corporate Lab, School of Mechanical and Aerospace Engineering, Nanyang Technological University, Nanyang Avenue 50, Singapore 639798, Singapore
[2]Singapore Centre for 3D Printing, School of Mechanical and Aerospace Engineering, Nanyang Technological University, Nanyang Avenue 50, Singapore 639798, Singapore
[3]3D Lab, HP Labs, HP Inc., Palo Alto, California 94304, USA

[a)]**Author to whom correspondence should be addressed:** kzhou@ntu.edu.sg

ABSTRACT

Freshwater scarcity is a pressing issue worldwide, and solar steam generators (SSGs) have emerged as a promising device for seawater desalination, harnessing renewable solar energy to facilitate sustainable water evaporation. The facile fabrication approach for SSG with complex topologies to achieve high water evaporation efficiency remains a challenge. Herein, a MIL-101 (Fe)-derived C@Fe_3O_4 ink was employed to multi-jet fusion (MJF) printing of polymeric porous SSGs with specific topologies. The optimized porous structure endows the printed SSGs with capillary force, greatly promoting water transport. The tree-like topology enables high water evaporation rates under various simulated solar radiation conditions. A finite element model was built to fully understand the light-to-thermal energy conversion and water evaporation processes. Moreover, the MJF-printed SSGs exhibit self-cleaning properties and can automatically remove accumulated salt on their surfaces, enabling sustainable desalination. During prolonged testing, the water evaporation rate of the SSGs remained relatively stable and reached as high as 1.55 kg m^{-2} h^{-1}. Additionally, the desalinated water met the standards for direct drinking water. This study presents a state-of-the-art technology for producing efficient SSGs for desalination and introduces a novel method for MJF printing of functional nanocomposites.

I. INTRODUCTION

Water scarcity is a significant problem in areas with increasing water consumption, caused by urbanization and the increasing demand for freshwater in households.[1] One solution to this problem is the desalination of seawater, which can be achieved through the application of solar steam generators (SSGs) or solar-driven water evaporators.[2–4] While the performance of SSGs depends heavily upon weather conditions and geographical location, their potential remains promising in numerous global regions, such as Singapore, Greece, and Saudi Arabia. There are three primary methods to increase the rate of water evaporation: raising the temperature of water, increasing the surface area of water, and accelerating surface air flow. SSGs use nonpolluting solar energy to improve the efficiency of seawater desalination mainly through the first two methods.

To enhance the steam generation efficiency, SSGs with high sunlight absorptivity and large specific surface area are desired.[5] Researchers are exploring the use of substances such as carbon-based nanomaterials and metallic nanomaterials (gold and metal oxides) with high absorbance in sunlight spectrum.[6–10] However, the use of powder nanomaterials in seawater evaporation must be approached with caution due to the complex recycling process and potential secondary pollution on water bodies. In addition, the commonly used subtractive manufacturing process for fabricating structures with large surface areas is relatively complicated, hindering the development and practical implementation of advanced SSGs. Therefore, the effective utilization of solar energy and converted heat and the feasible fabrication of SSGs with complicated structures are critical factors for developing practical SSGs for seawater desalination.

The combination of carbon-based nanomaterials and metal oxide nanoparticles has been scientifically validated as an effective approach for producing high-efficiency solar steam generation devices.[11,12] This approach combines the advantageous properties of carbon-based materials, including low cost, reusability, and a broad solar absorption spectrum. Nontoxic metal oxides, on the other hand, offer high conversion efficiency and chemical stability to the SSG devices.[13,14] Metal–organic frameworks (MOFs)-derived carbons, metal oxides, and carbon-encapsulated metal oxides have outstanding advantages in terms of ease of preparation, inherent diversity, and precise control of physicochemical properties.[15–19]

The high surface area and porosity of MOFs provide an ideal template for the synthesis of carbon-encapsulated metal oxides with a highly ordered hierarchical structure, which can significantly enhance sunlight absorption efficiency.[20–23] This theoretically leads to high solar-to-steam conversion efficiency and steam generation rate. Powder materials pose a challenge for recycling in real-world seawater desalination applications. They were deposited on the surface of fabrics or porous materials, limiting their ability to improve the efficiency by designing configurations or surface structures.[24,25] Therefore, finding a solution to effectively utilize these high-performance materials as SSGs has become a pressing issue.

Multi-jet fusion (MJF) is a powder bed fusion additive manufacturing technology, which can prepare complex products without external supporting structures, and shows high printing efficiency due to its inkjet printing mode.[26,27] The MJF printing process consists of three stages: powder spreading, ink jetting, and powder fusing. By repeating these cycles, products with the desired structure can be produced. The replaceable and modifiable fusing agents endow the black printed parts with a high light absorbency. Our previous work has demonstrated the feasibility of using functional inks as the fusing agents to enhance the functionality of printed parts.[28] The development of inks with good photothermal performance not only aids in the printing of high-quality products but also holds great promise for enhancing the light absorbance and photothermal conversion efficiency of the final product for SSGs applications. The combination of functionalized fusing agents and MJF printing shows promising potential for producing high-performance SSGs.

Nevertheless, the accumulation of salt on the SSGs surface under high working intensity, such as concentrated brine and strong solar irradiation, inevitably reduces the supply of water and the photothermal properties of the SSGs.[29,30] Solving this problem is the most important and difficult task to maintain sustainable performance of SSGs for seawater desalination. The self-cleaning mechanism of salts from SSGs surface can be divided into three parts, namely, mechanical removal, shielding effect, and force-driven fluid flow.[31] Among them, the force-driven fluid flow method is widely used because it can be realized through structural design.[32] Capillary force in porous materials is widely used in nature to drive water flow, which can be used to improve the self-cleaning efficiency of SSGs.[33,34] Acquiring capillary-structured SSGs through conventional subtractive manufacturing techniques demands intricate preparation procedures and specific structural designs, resulting in elevated production costs and hindering their widespread applicability.

Computer-aided design (CAD) facilitates the MJF printing of diverse and porous structures.[35,36] The recommended minimum feature size with standard MJF print quality is approximately 0.5 mm.[37] Internal cavities with such small size in printed porous parts present a challenge when attempting to clean unmelted powder from these surfaces. Consequently, producing capillary structures (continuous micrometer-scale pore structure) with MJF printing is difficult. One potential solution is to utilize pore-forming agents, such as water-soluble salts, polymers, and small organic molecules. These agents can facilitate the efficient creation of porous structures while improving the sustainability and environmental friendliness of the material, as they are recyclable.[38,39] To date, no reports have been made on MJF printing of porous materials with capillary structures. The utilization of CAD-assisted design and tailored material formulations enables the fabrication of capillary structures through MJF printing, rendering MJF a highly promising technology for SSG applications.

In this work, a photothermal ink, composed of water, surfactant, and MOFs-derived carbon encapsulated Fe_3O_4 ($C@Fe_3O_4$) hybrid, was synthesized and applied as the fusing agent for MJF printing. The porous SSGs with complex topologies were designed, printed, and applied for water evaporation and seawater desalination. Thermostable and low-toxicity sodium carbonate (Na_2CO_3) was applied as a porogen for printing porous polyamide 12 (PA12)-based parts with capillary structure. The characterization of the structures and morphologies of both the synthesized ink and printed SSGs was performed to optimize the material formulations. Based on the above-mentioned design schemes, a series of MJF-printed porous SSGs with special surface structures were prepared, which exhibited excellent photothermal performance and salt self-cleaning properties. This work offers a fast and easy preparation method for the fabrication of 3D SSGs with complex structures and high efficiency and has the potential to expand the application fields of MJF technology.

II. METHODOLOGY

A. Materials

$FeCl_3{\cdot}6H_2O$ and terephthalic acid were purchased from Sigma-Aldrich Pte. Ltd. The PA12 powder used for printing was HP 3D High Reusability PA12 with a median size of 52.6 μm and a peak melting temperature of 188.4 °C. Flow diagram with images of the process of the preparation of ink and porous SSGs was portrayed in Fig. S1.

B. Preparation of $C@Fe_3O_4$ ink

The precursor of $C@Fe_3O_4$ hybrids, MIL-101 (Fe) was synthesized from $FeCl_3{\cdot}6H_2O$ and terephthalic acid (mole ratio 2:1) in DMF solution. The mixture was transferred into a Teflon-lined stainless-steel autoclave and heated at 120 °C for 6 h. The obtained precipitates were collected by centrifugation and annealed at 800 °C for 3 h with the heating rate of 5 °C min^{-1} under nitrogen condition. The obtained black products are $C@Fe_3O_4$ hybrids. Certain hybrids were dispersed into 2 mg ml^{-1} PVP solution and treated with probe sonication for 1.5 h (250 W). Poorly dispersed $C@Fe_3O_4$ hybrids were removed by centrifugation at 3000 rpm for 30 min. Consequently, a well dispersed black $C@Fe_3O_4$ ink was prepared.

C. Preparation of porous PA12-based SSGs

A series of volume ratios between Na_2CO_3 and PA12 powder (20:80, 30:70, and 40:60, named as N_x/P_y, where N, P, x, and y denote Na_2CO_3, PA12, volume of N, and volume of P, respectively) were prepared for printing. Na_2CO_3 was milled at 300 rad/min for 10 min and

then sieved using a 300 meshes stainless steel sieve to screen the particles with sizes less than 50 μm. The mixed powders have great flowability and are suitable for MJF printing. Except that the fusing agent was replaced by C@Fe_3O_4 ink, other printing conditions were the same as pure PA12. The powder was spread on the print bed with a roller, and the ink was sprayed on the powder according to the design pattern. Under the irradiation of the IR lamp, the ink absorbed heat and melted the Na_2CO_3/PA12 powder to form a product unit. By stacking layer by layer, a Na_2CO_3/PA12 composite material with a unique structure was produced. To remove Na_2CO_3 in the composites to form porous structure, the fabricated parts were immersed in tap water and ultrasonically treated in water bath for 30 min (150 W). The obtained products were dried in an oven at 80 °C for later use.

D. Simulation

The heat and moisture air transfer process in the generator system are simulated by a finite element (FE) model built in the COMSOL Multiphysics software. As shown in Fig. 1, the established model has the same dimensions as one unit of the printed sample. The porous medium domain, free flow domain, and water domain are, respectively, drawn in purple, white, and gray. The height of the free flow domain and water domain are 10 times and 2 times the thickness of the porous SSG plate, respectively. It is noted that the height of the water domain is set at 0 if the SSG is not in direct contact with the water surface.

The temperature variation is solved by the energy equation as follows:

$$\rho c_p \frac{\partial T}{\partial t} + \rho c_p \mathbf{u} \cdot \nabla T + \nabla \cdot (-k \nabla T) = Q_{solar} + Q_{rad} + Q_{evap} + Q_{conv}, \quad (1)$$

where ρ is the material density, c_p is the heat capacity, and k is the thermal conductivity. The fluid velocity field $\mathbf{u}$ in the free flow domain and porous medium domain are solved by the Navier–Stokes equation and Brinkman equation, respectively. It is noted that the material properties of the porous medium depend on the concentrations of liquid c_l and vapor c_v which is solved by Fick's first law.

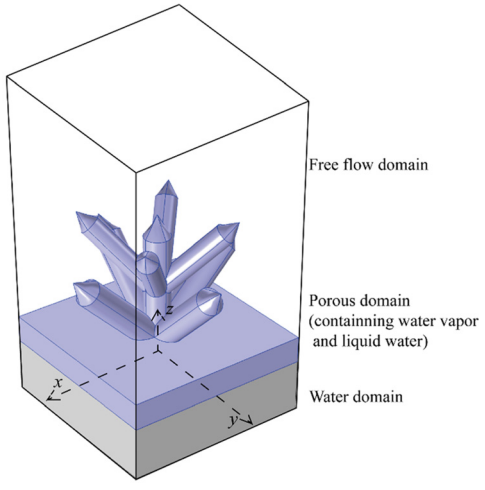

FIG. 1. Finite element model of one "tree" unit for the simulation of heat and moisture air transfer process. From top to bottom, the model comprises three computational domains, including the free flow domain, porous medium domain, and water domain.

As indicated in Eq. (1), there are four kinds of heat sources in this generator system, including the solar irradiation Q_{solar}, radiation loss Q_{rad}, heat evaporation Q_{evap}, and thermal convection Q_{conv}. The expressions of these heat sources are

$$\begin{aligned} Q_{solar} &= \alpha I_{solar} |\hat{n} \cdot \hat{z}|, \\ Q_{rad} &= \varepsilon \sigma (T^4 - T_0^4), \\ Q_{evap} &= H_v k_v (c_{sat} - c_v), \\ \text{and} \quad Q_{conv} &= h_{conv} (T - T_0), \end{aligned} \quad (2)$$

where α is the surface absorptivity, I_{solar} is the incident solar intensity, ε is the material emissivity, σ is the Stefan–Boltzmann constant, H_v is the heat of evaporation, k_v is the mass transfer coefficient, c_{sat} is the saturation vapor concentration, h_{conv} is the convective heat transfer coefficient, and T_0 is the environment temperature. All data used in this work are listed in Table S1.

Five moduli of COMSOL are generated together to simulate the above-mentioned equations. Specifically, the fluid heat transfer module is employed to simulate Eq. (2), while Q_{solar} and Q_{rad} are coupled to Eq. (2) by applying the surface-to-surface radiation module. The fluid velocity field is solved within the laminar flow module, and the transfer of liquid water and moist vapor in porous medium domain are determined by two dilute species transport moduli. In the current simulation, the calculation domain is segmented into 30 917 tetrahedral meshes with a maximum size of 0.0219 mm. The employed time step is 0.025 min. The applied computational domain, mesh size, and time step have been checked to ensure both high numerical accuracy and computational efficiency in the study.

E. Characterization

XRD patterns were recorded on Shimadzu 6000 x-ray diffractometer with Cu Kα radiation ($\lambda = 0.154$ nm) to investigate the crystalline structures of the materials. The powder sample was flattened in the designed holder and placed horizontally on the test bench. Transmission electron microscopy (TEM, JEM-2100F, Japan Electron Optics Laboratory Co., Ltd., Japan) was employed to investigate the micromorphology of MOF and C@Fe_3O_4 hybrids. To confirm the elementary composition of C@Fe_3O_4, x-ray photoelectron spectroscopy (XPS) was applied on the samples with a VG ESCALB MK-II Electron spectrometer (Al Kα excitation source at 1486.6 eV, Japan). The morphology of the fillers and fracture surfaces of the printed samples was characterized using a scanning electron microscope (SEM) (JSM-5600 LV, JEOL, Japan). The flowability of PA12 composite powder was investigated before printing by a flowability measurement instrument (Revolution Powder Analyzer, Basel, Switzerland). The avalanche angle was measured 250 times, and the rotation rate of the drum was 0.6 rpm. The mechanical properties of the printed samples were characterized by the Shimadzu AGX 10 kN universal tester at a crosshead speed of 10 mm min^{-1}. Five samples (ASTM D638 Type V standard) were measured for each group. The apparent viscosity of the agents was measured at a shear rate ramp from 0.1 to 100 s^{-1} by a rotational rheometer (DHR-2, TA Instruments, USA) with a parallel plate geometry of 40 mm in diameter. The temperature distribution of the powder

bed and printed parts was recorded by an infrared camera (A655sc, FLIR systems, Inc., USA).

III. RESULTS AND DISCUSSION

A. Characterization of inks

The schematic synthesis process of C@Fe_3O_4 ink for MJF printing is shown in Fig. 2(a). Well-dispersed hybrids in the water facilitated the fabrication of porous PA12-based SSGs via MJF printing [Fig. 2(b)]. The detailed preparation processes of porous SSGs are shown in Fig. S2(a). The capillary structure formed by the continuous pores can generate the surface tension force that promotes the upward flow of water.[40] Like how capillary forces facilitate water transport in plants, the presence of continuous micrometer-scale pores in the porous printed parts can promote water transport from the container to the surface of the SSGs [Fig. 2(c)]. To enable seawater desalination in natural environments, porous PA12 columns were constructed to support the SSG and draw water to the surface of the SSG. The columns help to prevent direct contact between the SSG and water surface, thereby reducing the propagation of heat toward the water and facilitating heat accumulation on the surface of the SSG. These capillary structures, combined with the SSG configuration, reduce thermal losses and improve the efficiency of water evaporation [Fig. 2(d)].

MIL-101(Fe) was prepared by reacting $FeCl_3 \cdot 6H_2O$ and 1,4-dicarboxybenzene as precursors. The resulting transmission electron microscopy (TEM) image in Fig. S2(b) revealed the formation of octahedral-shaped MIL-101(Fe) crystals with sizes around 2 μm, which exhibited a concave surface and confirmed the successful synthesis of the MOF.[41] A one-step-controlled calcination method was utilized to prepare the C@Fe_3O_4 hybrids. Due to the collapse of the crystal structure of the synthesized MOF, a morphologically aggressive transformation of MIL-101(Fe) was observed after the pyrolysis process. Energy-dispersive spectrometry (EDS) indicated that the sample was mainly composed of C, O, and Fe [Fig. S2(c)]. The TEM image displays the presence of opaque matrices (amorphous carbon) wrapped with black spots (magnetic Fe_3O_4 nanoparticles with an average diameter of around 50 nm) [Fig. 3(a)]. This constitution was confirmed by the enlarged TEM image [Fig. S2(d)], suggesting that Fe_3O_4 nanoparticles were embedded in the amorphous carbon. A high-resolution TEM (HRTEM) image in Fig. 3(b) provides further insight into the structural information on the building blocks. The HRTEM image clearly shows the lattice fringe with an interplanar spacing of 0.253 nm, assigning to the (311) crystal plane of Fe_3O_4.[42]

Figure 3(c) shows three characteristic powder x-ray diffraction (PXRD) peaks at $2\theta = 8.7°$, 19.7°, and 22.5°, which confirm the formation of MIL-101(Fe). These peaks match well with those reported in previous studies.[43,44] After annealing at 900 °C for 3 h, the original diffraction peaks were no longer observed, indicating a transformation of the crystalline structure into a new phase. The XRD peaks were located at 18.2°, 30.2°, 35.5°, 43.3°, 53.2°, and 56.7°, corresponding to (111) (220) (311) (400) (422), and (511) reflections of the cubic spinel structure, in accordance with the TEM results.[45] These peaks are consistent with the major peaks of Fe_3O_4 (JCPDS file No. 01-079-0419),[46] indicating that the Fe_3O_4 crystal structure resulted from the pyrolysis of MIL-101(Fe) to form a C@Fe_3O_4 hybrid.

The full x-ray photoelectron spectroscopy (XPS) spectra of the MIL-101 (Fe) and C@Fe_3O_4 nanomaterials are shown in Fig. S2(e). The degradation of organic parts in MOFs increased the mass ratio of Fe-containing compounds, as demonstrated by the increased atomic content of Fe from 5.89% for MIL-101 (Fe) to 10.13% for C@Fe_3O_4. Figure 3(d) presents the narrow scan XPS spectra of C 1s and Fe 2p in C@Fe_3O_4 hybrids. The C 1s spectrum can be deconvoluted into three components C=C/C–C (284.7 eV), C–O (286.1 eV), and C = O (288.9 eV), confirming the high content of C = C/C–C carbon, which benefits the light absorption.[47] The fitted peaks at 710.0 and 726.3 eV correspond to Fe $2p_{3/2}$ and Fe $2p_{1/2}$ of Fe^{3+}, while the fitted peaks at 708.6 and 724.1 eV correspond to Fe $2p_{3/2}$ and Fe $2p_{1/2}$ of Fe^{2+}, respectively, confirming the existence of Fe_3O_4 in the hybrids.[48–50] By utilizing XRD, XPS, and TEM, it is demonstrated that one-step-controlled calcination is a viable method for converting MIL-101(Fe) precursors into C@Fe_3O_4 hybrids.

The viscosity of the ink and the flowability of the powder are the key factors that determine the MJF printability of the formulations.[51] C@Fe_3O_4 ink has a similar viscosity with the commercial HP fusing

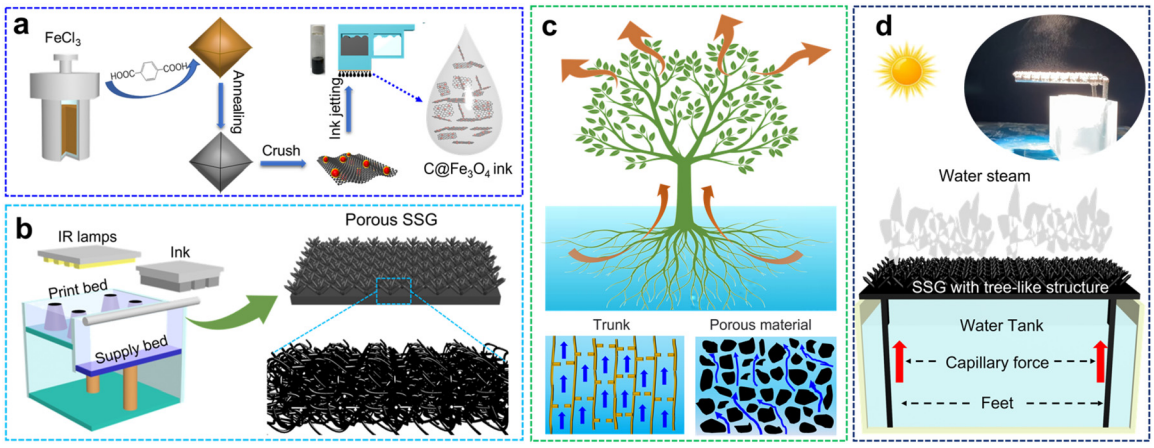

FIG. 2. The fabrication and application of MJF-printed SSGs. (a) Schematic synthesis process of the C@Fe_3O_4 ink for MJF printing. (b) Illustration of the MJF testbed setup and the structure of printed SSGs. (c) Schematic illustration of transpiration in plants and water transport in trunk and porous materials. (d) The illustrated evaporation process of water on the surface of MJF-printed SSG under solar irradiation.

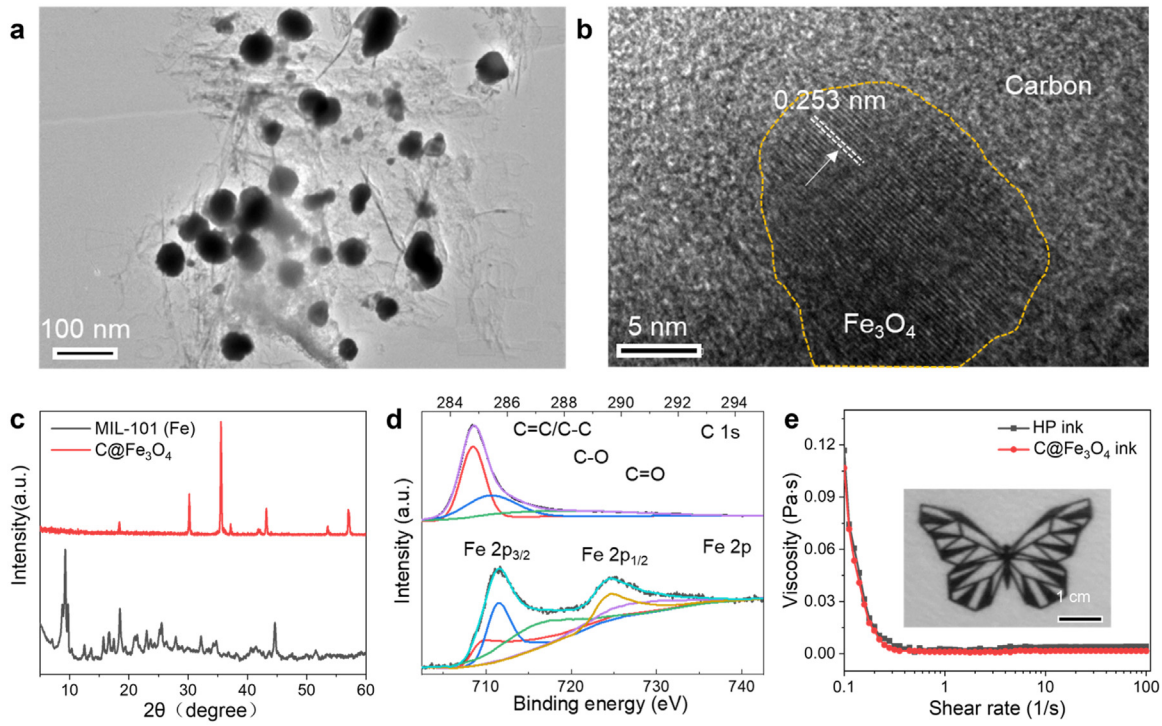

FIG. 3. The characterizations of C@Fe_3O_4 hybrid. (a) TEM image of C@Fe_3O_4 hybrid. (b) HRTEM image of C@Fe_3O_4 hybrid. (c) XRD curves of MIL-101 (Fe) and C@Fe_3O_4 hybrid. (d) High resolution Fe 2p and C 1s spectra and their fitting lines of C@Fe_3O_4 hybrid. (e) Viscosity of the C@Fe_3O_4 ink as a function of shear rate. The inserted digital image is a printed butterfly pattern via C@Fe_3O_4 ink.

agent (FA), since they have comparable concentration [Fig. 3(e)]. The value of the inverse Ohnesorge number Z is used to evaluate the ink droplet jetting behaviors and can be calculated by

$$Z = \sqrt{\rho\gamma d}/\eta, \tag{3}$$

where ρ, γ, and η denote the density, surface tension, and complex viscosity (at 100 s^{-1}) of the ink, respectively. The ρ of the commercial FA and synthesized C@Fe_3O_4 ink was 1.105 and 1.125 $g{\cdot}cm^{-3}$, respectively. The γ values for C@Fe_3O_4 ink and commercial FA were determined as 43.6 and 31.6 $mN{\cdot}m^{-1}$, respectively, using a contact angle meter. Based on the above-mentioned data, the Z value of the commercial FA and the C@Fe_3O_4 ink can be calculated as 7.959 and 3.173, respectively, within the range from 1 to 10, demonstrating that the ink droplet jetting will be stable.[52]

After being filled with the C@Fe_3O_4 ink, the cartridges were mounted on the MJF testbed for printing tests. As shown in the image inserted in Fig. 3(e), the ink is capable of printing the designed pattern, and the maximum resolution of the pattern could reach below 200 μm, which shows that the prepared ink has good printability. The photothermal properties of the designed ink are also important for MJF printing. Inks with good heat absorption performance can not only reduce the intensity of infrared light during printing but also improve the photothermal performance of the printed SSGs. The simulated solar irradiation device is a Xenon light source (HF-GHX-XE-300, Hefan, China), while the temperature of the sample is detected and recorded by an infrared camera (FLIR A6000, Teledyne Technologies, U.S.) [Fig. S2(f)].

Figure 4(a) shows the photothermal performance of the printed PA12 plate using the C@Fe_3O_4 ink under different irradiation intensities. The temperature of the PA12 plate could reach 47.3 °C in 100 s under 1 simulated solar irradiation (1 sun). In contrast, the corresponding temperature of the plate printed by commercial FA could only reach 42.1 °C [Fig. S2(g)], confirming the superior photothermal performance of the C@Fe_3O_4 ink. Additionally, the temperature decay profile after turning off the irradiation indicates that the C@Fe_3O_4 ink has a slower cooling rate, which can be advantageous in maintaining the temperature of printed SSGs.

The carbon coating on the surface of the Fe_3O_4 nanoparticles enhances their photothermal properties, leading to improved photothermal conversion efficiency [illustrated in Fig. 4(b)]. The C@Fe_3O_4 can efficiently absorb near-infrared light and convert it into heat, due to the combined effects of the carbon shell and Fe_3O_4 core. In addition, Fe_3O_4 has excellent stability and low toxicity, making it a safer option for water treatment applications compared to other photothermal agents.[53] The carbon shell also provides a protective barrier, shielding the iron oxide core from degradation, oxidation, and other unwanted reactions.[54] The use of a stable filler can reduce the adverse impact of SSGs on water safety.

To investigate the stability of the MJF-printed porous SSGs, they were immersed in both seawater and de-ionized water, respectively.

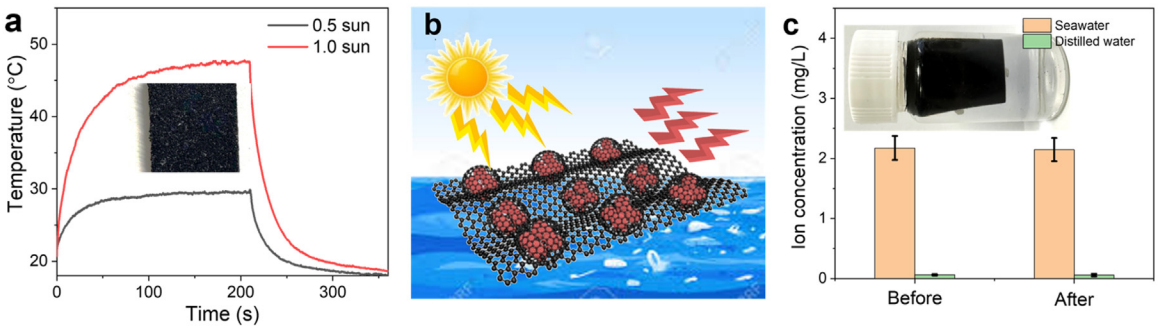

FIG. 4. The photothermal performance of MJF-printed SSGs. (a) The heating and cooling behavior of the dried ink (inserted digital image) under different simulated solar intensities. (b) Schematic diagram of the photothermal mechanism of C@Fe_3O_4 hybrid. (c) The concentration of iron ions in seawater before and after the samples were immersed for one month.

After being placed outdoors for one month, the concentration of Fe^{3+} ions in the liquids were monitored. As shown in the inserted graph [Fig. 4(c)], no black precipitate was observed in the seawater, and the Fe^{3+} ion concentration in both seawater and de-ionized water before and after immersion remained almost unchanged. This suggests that the prepared C@Fe_3O_4 ink can be safely utilized for MJF printing of polymeric SSGs for seawater desalination and water evaporation, without posing any potential hazards from the raw materials.

B. Characterization of printed samples

The PA12 powder used in this work had a median size of 52.6 μm and a peak melting temperature of 188.4 °C. While the average size of milled Na_2CO_3 powder was 24.6 μm [Figs. S3(a) and S3(b)]. The effect of powder formulation on its flowability can be characterized by an avalanche angle tester. When the powder in the container rotates with the motor, it will produce a collapse angle, that is, an avalanche angle. The larger the value of the avalanche angle α, the worse the fluidity of the powder [Fig. S3(c)].[55] Figure 5(a) shows that the flowability of composite powders deteriorates with the increase in Na_2CO_3 content. The peak value of α increased from 52.5° for pure PA12 to 67.5° for N_{50}/P_{50}. The avalanche angle of Na_2CO_3 was 65.3°, much higher than that of pure PA12 powder [Fig. S3(d)]. The small Na_2CO_3 particles fill the voids between PA12 powders and increase the density of composite powders, making the powder denser and more compact. Therefore, formulations with high Na_2CO_3 content are not suitable for MJF printing. The superior formulations in this work are N_{20}/P_{80} and N_{30}/P_{70}.

To verify the porosity of printed samples with different volume ratios of Na_2CO_3, the XRD, scanning electron microscope (SEM), and micro-computed tomography (Micro-CT) were applied. The Na_2CO_3 existed in N_{30}/P_{70} can be easily removed by ultrasonication at 150 W for 30 min. After sonication treatment, the sharp peaks of Na_2CO_3 disappeared in the XRD curve of porous PA12 [Fig. 5(b)].

There are some small and island-like holes within N_{20}/P_{80}, indicating no continuous holes formed in this formulation [Fig. S4(a)]. In contrast, continuous holes were observed in N_{30}/P_{70}, N_{40}/P_{60}, and N_{50}/P_{50} [Figs. 6(a) and 6(b) and S4(b) and S4(c)]. However, the skeletons became thinner with the decreasing volume ratio of PA12, which theoretically impaired the mechanical strength of porous products.

The voids existing inside the material inevitably deteriorate its mechanical properties. Nonetheless, thanks to the outstanding mechanical properties of PA12, even at high porosity levels (>30%), it can still satisfy the strength criteria for the application of SSGs. As shown in Fig. 6(c) and Table I, the tensile strength of porous SSGs decreased with the increasing porosity, that is, from 7.75 MPa for N_{20}/P_{80} to 1.16 MPa for N_{50}/P_{50}. The N_{30}/P_{70} component is significantly stronger than N_{40}/P_{60} and is better suited for practical applications. The voids in the matrix act as force concentration sites, thus weakening the ability of SSGs to resist external forces. Since the

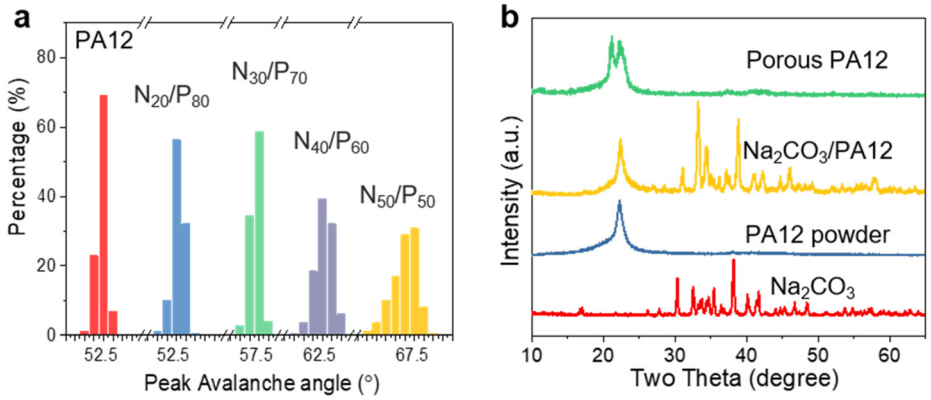

FIG. 5. Characterization of the MJF-printed SSGs. (a) Avalanche angle distribution histogram of PA12 composite powders fitted by Gaussian function. (b) PXRD curves of Na_2CO_3, PA12 powder, Na_2CO_3/PA12 powder composite, and printed SSG.

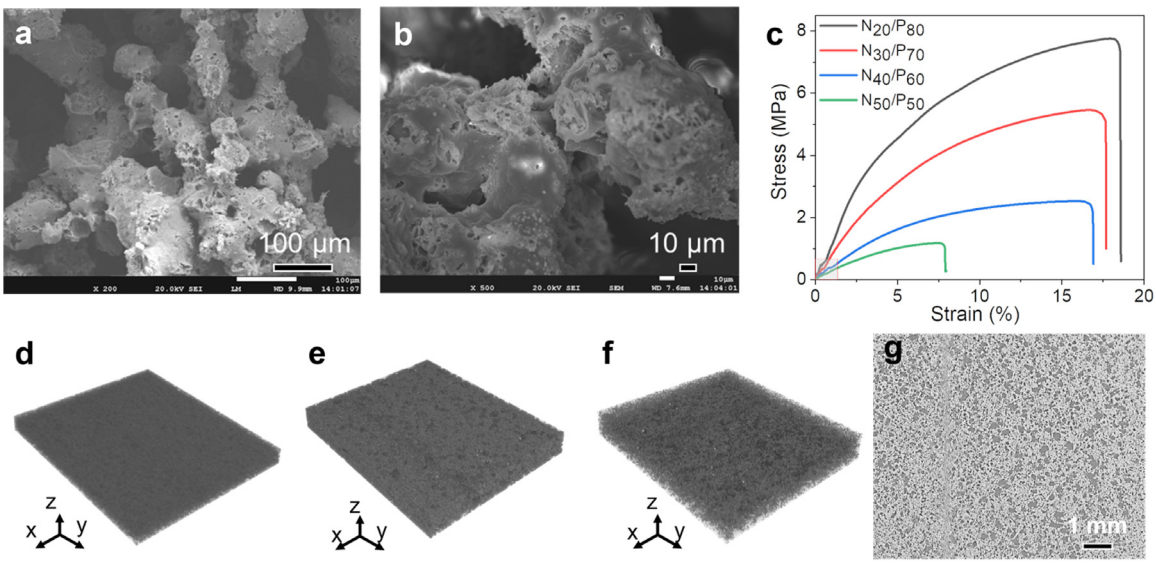

FIG. 6. Porosity control of the MJF-printed SSGs. SEM images of fractured surface of porous N_{30}/P_{70} under (a) low and (b) high magnifications. (c) Strain–stress curves of printed porous materials. The 3D micro-CT images of printed (d) N_{20}/P_{80}, (e) N_{30}/P_{70}, and (f) N_{40}/P_{60}. (g) The slice of N_{30}/P_{70} in horizontal direction.

TABLE I. The mechanical properties of porous PA12 with different porosity.

Sample	Porosity (%)	Tensile strength (MPa)	Young's modulus (GPa)	Elongation (%)
N_{20}/P_{80}	25	7.46 ± 0.29	1.11 ± 0.13	18.6 ± 3.1
N_{30}/P_{70}	37	5.44 ± 0.26	0.91 ± 0.09	17.7 ± 2.8
N_{40}/P_{60}	51	2.53 ± 0.47	0. 60 ± 0.01	11.9 ± 4.3
N_{50}/P_{50}	No data	0.93 ± 0.23	0.03 ± 0.01	5.6 ± 2.6

mechanical properties of N_{50}/P_{50} are too poor for practical use, only the other three formulations are considered for further investigation of the porosity of the product.

The microscopic difference in the structure directly affects the mechanical properties of the printed part. The inner holes of the printed parts were detected by Micro-CT, and the combined 3D constructions are portrayed in Figs. 6(d)–6(f). The transparency of the constructions increases with the content of porogen (Na_2CO_3), indicating the increasing porosity. The porosity of N_{20}/P_{80}, N_{30}/P_{70}, and N_{40}/P_{60} can be obtained by processing CT slices with the software ImageJ, which were 25%, 37%, and 51%, respectively. The horizontal slice of N_{20}/P_{80} confirmed the island-like structure of holes [Fig. S5(a)]. In contrast, small holes scattered in the full view of the slice for N_{40}/P_{60} and separated the PA12 skeletons [Fig. S5(b)], leading to poor mechanical performance. Micro-scale pores of relatively uniform size can be observed in horizontal sections of N_{30}/P_{70}, which allows for efficient transport of fluids while preventing unwanted materials from passing through [Fig. 6(g)]. All results above confirmed the superiority of the N_{30}/P_{70} formulation and the continuous pore structures in the corresponding printed sample. The distribution of pore sizes within the slices of the printed samples was quantified utilizing the ImageJ software. The related results are supplied in Fig. S5(c). The Na_2CO_3 particles were mixed with PA12 particles through mechanical mixer. Some particles flowed together with the melted polymers and, thus, generated holes larger than their original size. As the concentration of Na_2CO_3 increases, the pore size distribution within the samples shifts toward larger dimensions, which contributes to the deterioration of the mechanical properties of the samples.

The water affinity of printed parts affects the water transport during desalination. In theory, the high porosity and interconnected porous structure of the printed SSG result in large capillary forces that facilitate water penetration, thereby endowing it with good hydrophilic properties. The water contact test results shown in Figs. 7(a) and S6 clearly illustrate the excellent water affinity of the printed polymeric SSGs. Water droplets can easily permeate from the surface to the interior of the SSG (Videos 1 and 2). When the interior is wetted, this capillary action becomes more pronounced, and water droplets penetrate the interior in a very short time (less than 0.3 s), indicating improved hydrophilicity. Similar to the way in which trees and grasses absorb water via capillary forces [Figs. 7(b) and 7(c)], the rapid water absorption property of SSGs facilitates the drawing of seawater from low to high locations. Heat conduction is reduced as there is minimal direct contact between the SSG and seawater. This property also allows for the majority of photothermal energy to be utilized for seawater evaporation on the surface of SSGs. Theoretically, this feature could enhance the desalination efficiency of SSGs.

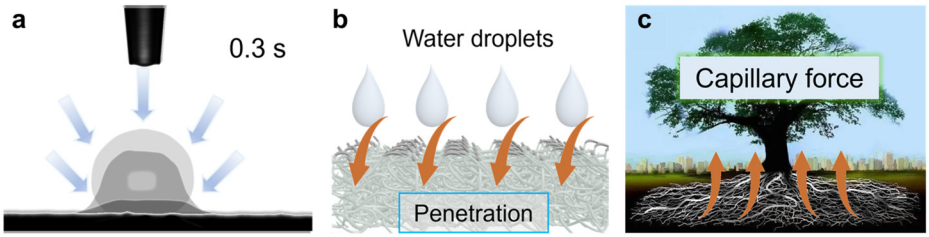

FIG. 7. Water behavior within MJF-printed SSGs. (a) Water affinity of the MJF-printed SSG plate. (b) Schematic illustration of the capillary force-driven water affinity mechanisms in the printed porous SSGs. (c) Capillary force facilitating water transport in plants.

C. Structural design

To determine the optical properties of printed porous SSGs, the reflection and transmission spectra of the samples ($2 \times 2 \times 0.05\ cm^3$) were measured using an ultraviolet-visible-near-infrared spectrophotometer. The results, as shown in Fig. 8(a), indicate that the porous SSG had a very low reflectance of less than 3.5% and almost no transmission in the range of 250–2500 nm, which covers most of the solar spectrum. These findings suggest that the porous SSG has the capacity to absorb a broad range of light, up to 96.7% of the incident solar energy. The rough surface architecture, porous structure, and the presence of C@Fe_3O_4 contribute to multi-scattering and light trapping effects that increase the optical path length of the incident light. As a result, solar energy conversion efficiency can be enhanced. To increase the surface area and promote the generation of interfacial solar steam, various three-dimensional structures (cone, cylindrical, and tree-like structure) were designed using CAD and fabricated upon the plate to investigate their steam generating capabilities [Figs. S7(a) and 8(b)]. The comparison on water evaporation performance of SSGs demonstrates that among these designs, the tree array structure, which consisted of multiple layers of branched small cones on a conical trunk, showed the most superior performance [Fig. S7(b)]. The tree array structure was manufactured using MJF printing to achieve one-step fabrication of SSG materials. The optical microscope images exhibit a typical tree-like structure with dimensions of approximately 16 mm^2 in area, 3 mm in height, and a base diameter of approximately 0.8 mm. The structure consists of eight 45° inclined conical branches located at the bottom and halfway up the tree. The minimum size of the conical structure at the tip is approximately 200 μm, and the porous feature is clearly visible. This porous feature is beneficial for achieving effective water transport within the matrix.

The temperature–time curve shows the increase in the temperature of the porous SSG plate under different irradiation intensities [Fig. S8(a)]. Clearly, as the light intensity increased, the stable temperature also increased. The SSG plate could reach a temperature of 44.03 °C under 1 sun, which is a practical device for water evaporation. Figure S8(b) compare the temperature distribution under 5 sun between the SSG plate and the tree-like structure (tree-structured SSG). The surface temperature of tree-structured SSG increased with the raise of irradiation intensity, but obviously higher than that of SSG plate at the same condition [Fig. 8(c)], demonstrating the tree-like

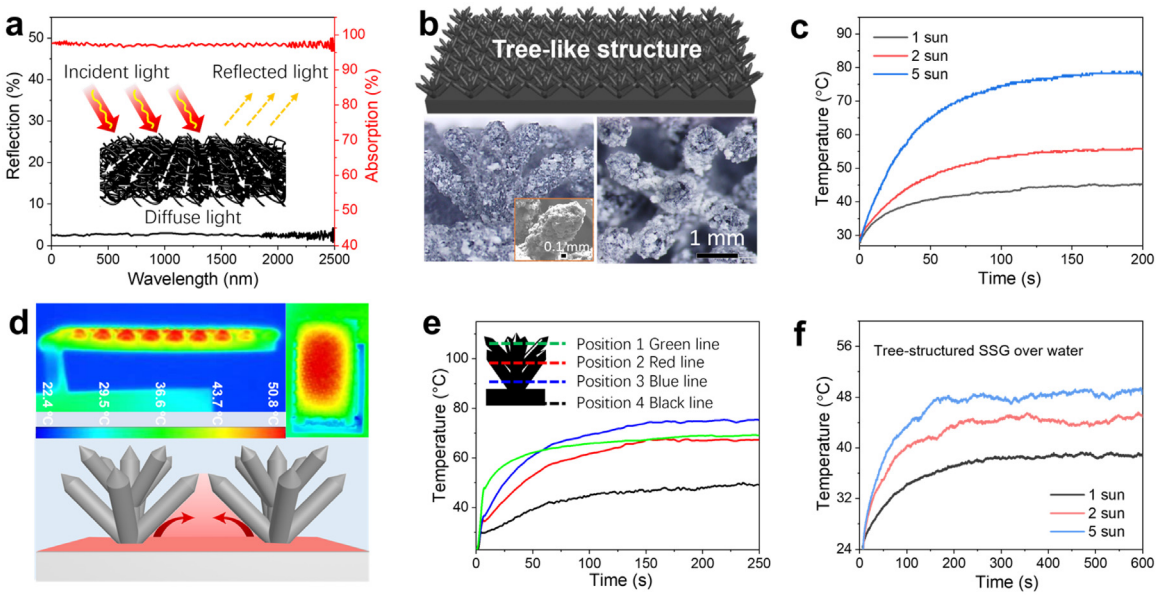

FIG. 8. Structural design and photothermal performance of tree-structured SSG. (a) Solar reflection and absorption curves of MJF-printed porous SSG, inserted the absorption mechanism of a porous material. (b) 3D model of the tree-like structure (up) and its optical images (bottom). (c) The heating behaviors of the tree-structured SSG under various solar irradiation intensities. (d) Side view and top view of the printed tree-like structure obtained via IR camera. (e) Temperature variations across different locations of tree-structured SSG. (f) The heating behaviors of the tree-structured SSG above water under various solar irradiation intensities.

surface topology has superior light absorption efficiency. A dense forest of the tree array was arranged on the surface of the platform to enhance the absorption of light radiation, thereby facilitating the heating and evaporation of seawater at the interface [Fig. 8(d)]. The gaps beneath the tree array structure can effectively block the dissipation of heat, allowing heat to accumulate at the bottom of the tree array and raise the temperature of the SSG, which is beneficial for achieving faster water evaporation.[56,57]

The tree-like structure on its surface has negligible influence on the water affinity, as confirmed by water contact angle test and high-speed camera (Fig. S9). Water droplets can easily permeate into the inner space of the tree-structured SSG as that of SSG plate. After absorbing water, the temperature distribution difference between the two configurations of SSGs becomes more pronounced. The high-temperature area only exists on the surface of the SSG plate but can penetrate deep into the interior of the tree-like structure in tree-structured SSG [Figs. 8(f) and S10(a)]. When subjected to the same light intensity, the tree-structured SSG can achieve a higher temperature than the SSG plates. Additionally, when placed above water, the temperature of the SSG is higher than that of the SSG plates on water [Figs. S10(b)–S10(e)]. Considering the significantly larger specific surface area of the tree-like structure, this feature will be beneficial for enhancing the evaporation rate.

Tree-like structures allowed more heat consumption through increased SSG–air interface and minimized the energy dissipated to the SSG underneath the plate surface, thus improving their energy efficiencies. To fully understand the light-to-thermal energy conversion and water evaporation processes, the heat and moisture air transfer process in the generator system are simulated by a finite element model built in the commercial software COMSOL Multiphysics 6.0. The established model has the same dimensions as one unit of the printed samples and is subjected to normal incidence irradiation from the light in the solar simulator. More details on the simulation can be found in the supplementary material. The placement of plate SSG and tree-structured SSG improved the water temperature, consistent with experimental results [Figs. 9(a) and 9(b) and S11(a)–S11(c)]. The predicted temperature distribution of tree-structured SSG closely aligns with the experimental results, whether in the cases on water or above water. above water is in good agreement with the experimental results [Fig. S11(d)], demonstrating a remarkable accuracy of this simulation method.

Due to structural shadowing and changed light incident angle, the equilibrium surface temperature will be affected by surface microstructures. The simulated outcomes and experimental results confirmed that the tree-like structure not only exhibits no detrimental impact on surface temperature beneath designed configuration but demonstrates the ability to augment its temperature [Fig. 9(c)]. The feature can be ascribed to the heat consumption caused by water evaporation process. No water was on the top of tree-like structures but accumulated beneath it [Fig. 9(d)]. Similar to transpiration of plants, the water that has been heated at the bottom of tree-structure SSG is continuously transported to the surface of the microstructure and escaped in the form of steam. The evaporation of water takes away a large amount of heat, generating low temperature on the surface but high temperature beneath the microstructure. Therefore, the tree-like structure optimizes the utilization of capillary forces for water absorption and, thus, enhances the sustainability of water evaporation.

D. Water evaporation performance of SSGs

The SSGs equipped with support columns can generate a large amount of vapor in a very short time (<10 s) [Fig. 10(a), Videos 3 and 4]. As depicted in the infrared image from the side view, the solar thermal energy is efficiently utilized as the heat concentrates on the surface of the SSG without diffusing downwards through the columns. Compared with the SSG plate, the tree-structured SSG can produce more vapor, indicating that it has a higher seawater evaporation rate [Figs. S12(a)–S12(e)]. The water evaporation tests were performed under different solar irradiation intensities (1 sun, 2 sun, and 5 sun) with water and seawater [Fig. S12(f)]. Figures 10(b) and 10(c) and S13 demonstrate the superiority of the tree-like structures in promoting water evaporation. The detailed data can be seen in Table S2. The water evaporation rate E values of different SSG materials are arranged in order: SSG plate < tree-structured SSG < SSG plate above water < tree-structured SSG above water. The tree-like structure improves water evaporation efficiency, as evidenced by the higher rate of water evaporation compared to the SSG plate under dark conditions (Fig. S14). This can be attributed to the increased contact area between water and air resulting from the tree-like structure, which enhances the evaporation of water.

Placing the SSG above the water leads to a significant increase in the E value compared to placing it on the water. This outcome aligns

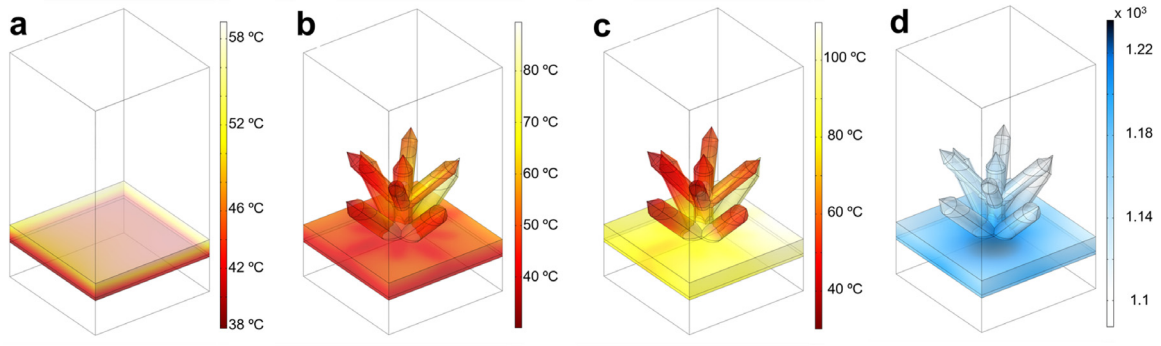

FIG. 9. Simulation results of cases under 5 sun. The surface temperature distribution of (a) pure water, (b) printed tree-structured SSG on water, and (c) tree-structured SSG above water. (d) The water distribution in tree-structured SSG above water.

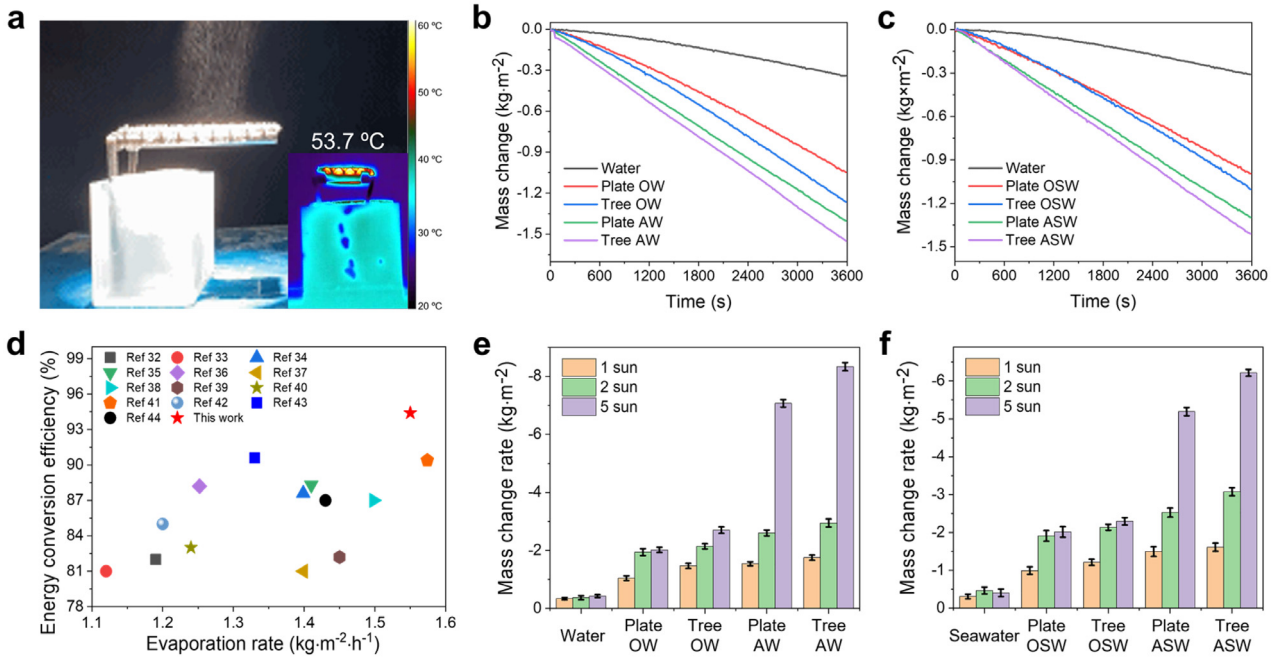

FIG. 10. Water evaporation test of the MJF-printed SSGs. (a) Tree-structured SSG above water during test under 5 sun. Plot of the weight loss through (b) water and (c) seawater evaporation under solar illumination as a function of irradiation time. (d) Comparison on energy conversion efficiency and evaporation rate between published papers and this work, tested under 1 solar irradiation intensity. (e) Water and (f) seawater evaporation rate of printed SSG samples under different solar irradiation intensities. "Plate" and "Tree" denote SSG plate and tree-structured SSG, respectively. "O," "A," "W," and "SW" mean on, above, water, and seawater, respectively.

with anticipated results, primarily because the separation of the SSG from water reduces heat dissipation, enhancing the efficiency of photothermal energy utilization. Under 1 sun irradiation, the highest E value was obtained by tree-structured SSGs placed above water, as high as 1.55 kg m^{-2}·h^{-1}. In contrast to this, the value of E for seawater under 1 sun irradiation was 1.41 kg·m^{-2}·h^{-1}. Overall, the water evaporation rate of water was slightly higher than that of seawater, due to the high concentration of ionic salts in seawater requiring more heat for evaporation.[30,58] With the increasing irradiation intensity, the evaporation rate increased sharply. The support structure provides enough water for transpiration on the surface of SSGs, even at 5 sun.

The energy conversion efficiency η of printed porous SSGs can be calculated by[59]

$$\eta = m h_{Lv} / C_{opt} q_i, \tag{4}$$

where m denotes the evaporation rate (the rate of water evaporation under the dark conditions is subtracted), q_i is the nominal solar irradiation, 1 kW m^{-2}, and C_{opt} is the multiple of 1 sun. h_{Lv} denotes total enthalpy of liquid–vapor phase change (including sensible heat and phase-change enthalpy), which can be calculated as

$$h_{Lv} = \lambda + C\Delta T, \tag{5}$$

where λ is the heat of water vaporization (varying from 2441.7 kJ·kg^{-1} at 25 °C to 2265.4 kJ kg^{-1} at 100 °C), C is specific heat capacity of water, 4.182 kJ kg^{-1}·$°C^{-1}$, and ΔT denotes the temperature increase in the water. The conversion efficiencies of the SSGs under 1 sun were 67.2%, 81.1%, 85.2%, and 94.4% for SSG plate on water, tree-structured SSG on water, SSG plate above water, and tree-structured SSG above water, respectively.

These results not only compare favorably to reported polymeric SSGs but also outperform the majority of data [Fig. 10(d) and Table II). The fabricated evaporator demonstrates significant improvements in the evaporation rate and energy utilization, which can be attributed to several key features. The hierarchical porous tree-like structure of SSGs provides a light-trapping effect, while the C@Fe_3O_4 hybrids broaden the light absorption bandwidth and enhance the conversion efficiency of light to heat. Moreover, the evaporation interface is fully detached from the water, enabling effective localization of the converted heat within the porous structure. This results in a high efficiency of photothermal-driven water-to-steam generation. As the intensity of light radiation increases, the rate of water evaporation also increases [Figs. 10(e) and 10(f)], indicating that the porous SSG prepared maintains good photothermal properties under strong light intensity.

During seawater desalination processes, the printed SSGs demonstrated effective self-cleaning performance against salt accumulation. Following 8 h of uninterrupted exposure to 1 sun illumination, the surface of the SSG exhibited the accumulation of white salts resulting from the evaporation of seawater (Fig. 11). Upon cessation of light exposure, the deposited salt on the SSG surface gradually diminished until they completely disappeared. This phenomenon indicates that the SSG printed by MJF has the function of salt self-cleaning. This phenomenon can be attributed to the water flow propelled by capillary force as well as the concentration difference between the region of high salt concentration on the SSG surface and the water in the container.

TABLE II. Comparison of the structure, preparation method, and water evaporation performance of several reported polymeric SSGs.

Polymer	Structure	Preparation method	Using mode	m (kg·m^{-2}·h^{-1})	η (%)	Reference
Oligoanilines	NaCl template foam	Polymerization	Bulk	1.1902	82.0	60
Cellulose	Aerogel	Freeze dry	Bulk	1.12	81	61
Polystyrene	Foam	Freeze dry	Bulk	1.3986	87.6	62
Polypyrrole (PPy)	Foam	Freeze dry	Bulk	1.41	88.3	63
Polyolefin elastomer	PEO-templated Foam	Melt blending	Bulk	1.252	88.2	64
Microporous polymer	Aerogel	Polymerization	Bulk	1.399	81	65
PPy-sodium alginate	Foam	Freeze dry	Bulk	1.498	87	66
Poly(vinyl alcohol)	Hydrogel	Freeze-and-thaw	Bulk	1.45	82.2	67
Nylon 6	Film	Electrospinning	Bulk	1.24	83	68
Melamine foam	Foam	Deposition	Bulk	1.574	90.4	69
Attapulgite polymer	Aerogel	Freeze dry	Bulk	1.2	85	70
Polyurethane sponge	Foam	Deposition	Bulk	1.43	87	71
Cellulose/alginate	Hydrogel	3D printing	Grid structure	1.33	90.6	72
Porous PA12	Na_2CO_3 template foam	3D printing	Tree-like structure	1.55	94.4	This work

As the accumulated salt dissolves in the surface water, a high-concentration brine is formed. Salt ions on the SSG surface are then transferred to the low-concentration side through diffusion until a concentration equilibrium is reached. During this process, the accumulated salt on the surface is gradually reduced until it is completely dissolved.

To further verify the stability of this property, we increased the solar intensity to 5 sun and used a high-concentration NaCl solution (25 wt. %), which resulted in more salt accumulation on the printed SSG surface (Fig. S15). The surface of SSGs completely turned white after 1.5 h of irradiation. After a certain period of time following the removal of the lamp, the salt on the surface of the SSG can be completely removed, and the tree-like structure of the SSG enhances this self-cleaning property, facilitating the removal of surface salt. This result indicates that the MJF-printed SSGs have a good salt self-cleaning function. This is of great significance for the application of SSGs, because the accumulated salts hinder the water transfer and affect the photothermal performance of SSGs, reducing the desalination efficiency. With their self-cleaning property, SSGs are able to undergo a cleaning process at night after being in operation during the day, without compromising their photothermal performance and seawater evaporation efficiency. This results in a sustainable desalination process.

E. Sustainable desalination of SSGs

To assess the practical applicability of the SSG material for outdoor desalination, a solar desalination device was designed and fabricated [Fig. 12(a)]. The device had a height of $20 \times 40 \times 20$ cm^3 and was constructed using a 3 mm thick transparent polymethyl methacrylate plate. The polymeric SSG was placed into the device, and steam generated by the SSG condensed on the top plate. The condensed water was collected at the bottom of the container. The SSG material used in this desalination device had an area of 50 cm^2. When the container was placed outdoors at 10:00 a.m. (1100 W m^{-2}) and retrieved at 1:00 p.m., it was observed that the previously transparent container walls were covered with water droplets after only 3 h. This demonstrates the excellent trial application ability of the designed SSG.

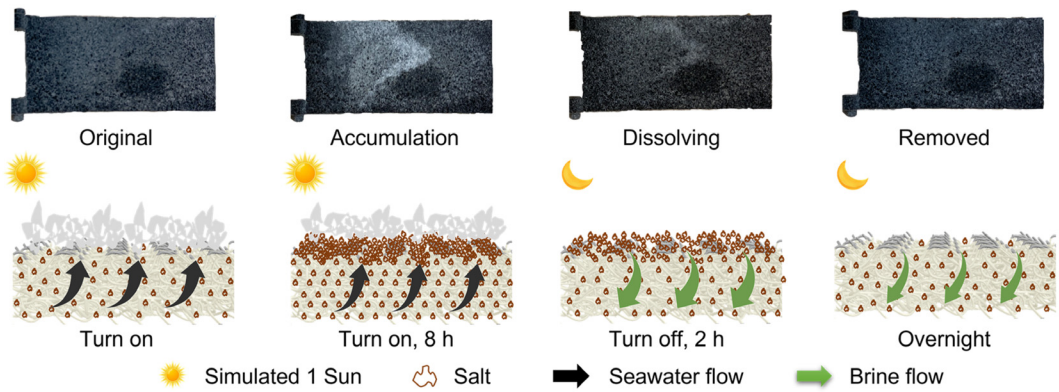

FIG. 11. Salt self-cleaning performance (up) and corresponding illustrated self-cleaning process (bottom) of the SSG plate under 1 solar irradiation intensity with seawater.

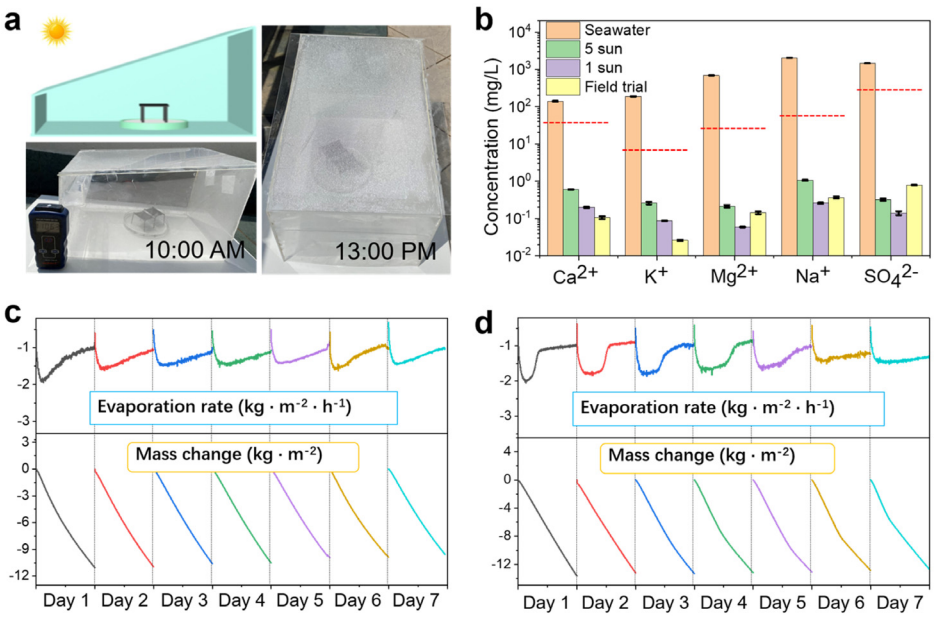

FIG. 12. Long-term water evaporation performance of the MJF-printed SSGs. (a) A closed container for field-trial testing of the tree-structured SSG. (b) Ion concentrations in seawater and recycled water collected under various solar irradiation intensities. One-week water evaporation performance of (c) SSG plate and (d) tree-structured SSG.

The ion concentration of the collected water was analyzed to verify whether it met the standard for direct drinking. Compared with the high concentrations of ions in seawater, the content of anions and cations in the desalinated water decreased by over 99.99%, meeting the WHO standard for drinking water [Fig. 12(b)]. Even water collected under high solar irradiation intensity can still meet the standards for safe consumption, confirming the well-performance of sustainable seawater desalination. Therefore, the desalinated water is considered sufficiently clean for daily use. Furthermore, a thorough comparison regarding the cost, manufacturing scalability, and environmental impact is provided in Table S3. This comprehensive analysis demonstrates that the utilization of MJF rapid 3D printing substantially reduces the production time and cost of SSG materials, rendering them more cost-effective than other photothermal materials. Amid the escalating global water scarcity crisis, there is an imperative demand for innovative and sustainable technologies for water purification and desalination. Our solar steam generators, characterized by their high water evaporation rate, offer a viable solution for the production of potable water from non-potable sources, such as seawater and brackish water, thereby addressing a critical dimension of water scarcity. These generators are designed for versatile deployment across various scenarios within existing water supply frameworks, including in remote locales bereft of access to centralized water treatment facilities, as well as in regions where conventional desalination processes are economically prohibitive or environmentally unsustainable. Furthermore, addressing potential challenges related to the implementation of this technology necessitates the development of infrastructure for the collection and distribution of purified water. It is also essential to engage local communities and build their capacities, ensuring the long-term sustainability and efficacy of the technology.

To assess the durability of the SSG apparatus and evaluate the impact of the tree-like structures on the performance of the SSG and the stability of the seawater desalination process, a one-week test was conducted under simulated sunlight for 9 h per day. The results of this test, comparing the SSG plate with the tree-like SSG structure, are presented in Figs. 12(c) and 12(d), respectively. During the one-week test, there was no significant change observed in the seawater desalination capacity and rate for the SSG with the tree-like top cover. In contrast, the desalination capacity of the SSG plate dropped remarkably by 10%. Overall, the tree-like top-layer structure not only significantly enhanced the seawater desalination capacity, resulting in more substantial mass loss, but also notably improved the durability of the SSG. The seawater desalination efficiency of both SSG configurations initially increased and then reached a stable level. This phenomenon could be attributed to the accumulation of halides on the sample surface after prolonged exposure to light, which caused salt precipitation and blocked the capillary action, resulting in a decrease in capillary force and hindering the rapid supply of seawater. Nonetheless, thanks to the self-cleaning effect, the accumulated salt in the capillary channels could be removed, minimizing impact on subsequent usage. This indicates that the prepared SSG is capable of operating for extended periods. Specific data regarding the mass loss of seawater and the water evaporation rate can be found in Table S4.

To assess the commercial applicability of the powder formulation proposed in this study, the MJF 5200 printing technology was employed to fabricate tree-structured SSGs using an HP fusing agent. The fabrication process successfully produced large-area SSGs with intricate structures, thus confirming the substantial potential for practical application of these SSGs [Fig. 13(a)]. Furthermore, the fabricated SSGs demonstrated promising performance in seawater desalination, as evidenced by the obtained results [Fig. 13(b)]. Specifically, when the tree-structured SSGs were utilized, one liter of seawater was entirely evaporated, whereas in the absence of the SSGs, approximately 500 ml remained unconsumed. The massive C@Fe_3O_4 ink will be synthesized in the future and applied for commercial MJF printing, which will further improve the water evaporation performance of large-area SSGs. Moreover, the integrated structure of SSGs fabricated by MJF presents opportunities for recycling and material reuse after prolonged use.

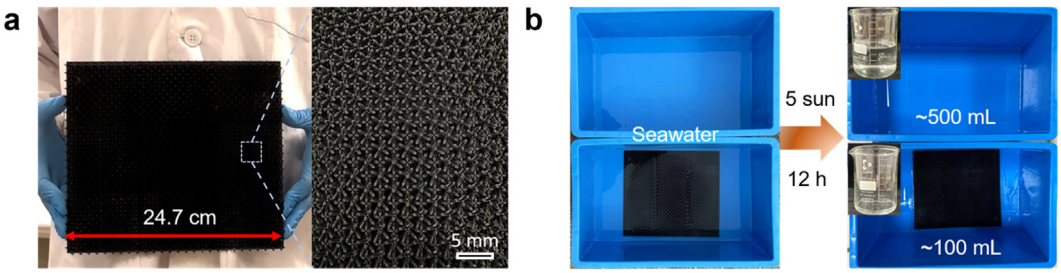

FIG. 13. Water evaporation performance test of a large-area SSG. (a) Tree-structured SSG printed by commercial printer MJF 5200. (b) The water evaporation test of printed large-area tree-structured SSG under 5 sun for 12 h.

Recycled SSGs could probably be ground into a powder form and re-fabricated through MJF, which worth further investigation. This potential recycling, if realized, would not only mitigate the environmental impact due to the minimized discards by minimizing discards but also significantly reduce raw material costs. Therefore, the SSG devices show great potential for practical applications in seawater desalination.

IV. CONCLUSION

In this study, MOFs-derived C@Fe_3O_4 hybrid was developed and used as the fusing agent for MJF printing to create SSGs with complex surface topologies. The photothermal properties, water evaporation rate, and salt self-cleaning ability of the material were assessed. The outcomes demonstrate that C@Fe_3O_4 nanoparticles display remarkable photothermal performance and can be employed in conjunction with MJF printing to manufacture robust and reliable SSGs. Moreover, we discovered an optimal material formulation that incorporates a capillary structure, which is pivotal in producing SSGs possessing superior hydrophilic properties. The water evaporation experiments revealed that the tree-structured SSGs considerably enhance the water evaporation rate, for both fresh and seawater, rendering them exceptionally well-suited for desalination applications. Furthermore, the unique porous structure of the SSGs generates capillary forces that can eliminate salt accumulation, resulting in exceptional self-cleaning performance. This enhances the sustainability of seawater desalination processes. The long-term seawater desalination tests showed that the SSGs prepared in this study can effectively produce potable water that meets WHO requirements.

However, it is noteworthy that given the current lab-scale scope of this work, further evaluation through pilot and industrial-scale tests is necessary for a comprehensive validation of the proposed approach. In summary, this interdisciplinary approach, which incorporates nanomaterials science, advanced additive manufacturing technologies, and surface structural design, presents a promising solution for the practical implementation of efficient SSGs.

SUPPLEMENTARY MATERIAL

See the supplementary material for synthesis detail and characterization of the nanowire and for Figs. S1–S15 and Tables S1–S4.

ACKNOWLEDGMENTS

This study was supported under the RIE2020 Industry Alignment Fund—Industry Collaboration Projects (IAF-ICP) Funding Initiative, Singapore, as well as cash and in-kind contribution from the industry partner, HP Inc.

AUTHOR DECLARATIONS

Conflict of Interest

The authors have no conflicts to disclose.

Author Contributions

Yanbei Hou: Conceptualization (lead); Data curation (lead); Formal analysis (equal); Investigation (equal); Writing – original draft (equal). **Ming Gao:** Investigation (equal); Writing – review & editing (equal). **Xueyu Bai:** Conceptualization (equal); Investigation (equal). **Lihua Zhao:** Resources (lead); Supervision (equal). **Hejun Du:** Supervision (equal). **Kun Zhou:** Project administration (lead); Supervision (lead).

DATA AVAILABILITY

The data that support the findings of this study are available within the article and its supplementary material.

REFERENCES

[1]M. T. van Vliet, M. Flörke, and Y. Wada, "Quality matters for water scarcity," Nat. Geosci. **10**(11), 800–802 (2017).
[2]V.-D. Dao, N. H. Vu, and S. Yun, "Recent advances and challenges for solar-driven water evaporation system toward applications," Nano Energy **68**, 104324 (2020).
[3]I. Ibrahim, D. H. Seo, A. M. McDonagh, H. K. Shon, and L. Tijing, "Semiconductor photothermal materials enabling efficient solar steam generation toward desalination and wastewater treatment," Desalination **500**, 114853 (2021).
[4]Y. Zhang, Y. Wang, B. Yu, K. Yin, and Z. Zhang, "Hierarchically structured black gold film with ultrahigh porosity for solar steam generation," Adv. Mater. **34**(21), 2200108 (2022).
[5]Z. Wang, H. Liu, F. Chen, and Q. Zhang, "A three-dimensional printed biomimetic hierarchical graphene architecture for high-efficiency solar steam-generation," J. Mater. Chem. A **8**(37), 19387–19395 (2020).
[6]M. Amjad, G. Raza, Y. Xin, S. Pervaiz, J. Xu, X. Du, and D. Wen, "Volumetric solar heating and steam generation via gold nanofluids," Appl. Energy **206**, 393–400 (2017).
[7]X. Hu, W. Xu, L. Zhou, Y. Tan, Y. Wang, S. Zhu, and J. Zhu, "Tailoring graphene oxide-based aerogels for efficient solar steam generation under one sun," Adv. Mater. **29**(5), 1604031 (2017).
[8]W. Li, Z. Chen, H. Yu, J. Li, and S. Liu, "Wood-derived carbon materials and light-emitting materials," Adv. Mater. **33**(28), 2000596 (2021).
[9]T. T. Pham, T. H. Nguyen, T. A. H. Nguyen, D. D. Pham, D. C. Nguyen, D. B. Do, H. V. Nguyen, M. H. Ha, and Z. H. Nguyen, "Durable, scalable and

affordable iron (III) based coconut husk photothermal material for highly efficient solar steam generation," Desalination **518**, 115280 (2021).
[10]J. Wang, Y. Li, L. Deng, N. Wei, Y. Weng, S. Dong, D. Qi, J. Qiu, X. Chen, and T. Wu, "High-performance photothermal conversion of narrow-bandgap Ti_2O_3 nanoparticles," Adv. Mater. **29**(3), 1603730 (2017).
[11]A. H. Elsheikh, S. W. Sharshir, M. K. A. Ali, J. Shaibo, E. M. Edreis, T. Abdelhamid, C. Du, and Z. Haiou, "Thin film technology for solar steam generation: A new dawn," Sol. Energy **177**, 561–575 (2019).
[12]K. W. Tan, C. M. Yap, Z. Zheng, C. Y. Haw, P. S. Khiew, and W. S. Chiu, "State-of-the-art advances, development, and challenges of metal oxide semiconductor nanomaterials for photothermal solar steam generation," Adv. Sustainable Syst. **6**(4), 2100416 (2022).
[13]F. Wang, D. Kozawa, Y. Miyauchi, K. Hiraoka, S. Mouri, Y. Ohno, and K. Matsuda, "Considerably improved photovoltaic performance of carbon nanotube-based solar cells using metal oxide layers," Nat. Commun. **6**(1), 6305 (2015).
[14]H. Wang, X. Mi, Y. Li, and S. Zhan, "3D graphene-based macrostructures for water treatment," Adv. Mater. **32**(3), 1806843 (2020).
[15]S. Guo, M. Gao, W. Zhang, F. Liu, X. Guo, and K. Zhou, "Recent advances in laser-induced synthesis of MOF derivatives," Adv. Mater. **35**, 2303065 (2023).
[16]X. Li, S. Zheng, L. Jin, Y. Li, P. Geng, H. Xue, H. Pang, and Q. Xu, "Metal-organic framework-derived carbons for battery applications," Adv. Energy Mater. **8**(23), 1800716 (2018).
[17]Y. Li, Y. Xu, W. Yang, W. Shen, H. Xue, and H. Pang, "MOF-derived metal oxide composites for advanced electrochemical energy storage," Small **14**(25), 1704435 (2018).
[18]X. Xu, J. Liu, J. Liu, L. Ouyang, R. Hu, H. Wang, L. Yang, and M. Zhu, "A general metal-organic framework (MOF)-derived selenidation strategy for in situ carbon-encapsulated metal selenides as high-rate anodes for Na-Ion batteries," Adv. Funct. Mater. **28**(16), 1707573 (2018).
[19]W. Yang, X. Li, Y. Li, R. Zhu, and H. Pang, "Applications of metal–organic-framework-derived carbon materials," Adv. Mater. **31**(6), 1804740 (2019).
[20]A. Li, Y. Wan, Y. Gao, Z. Tang, J. Xu, M. Huang, Y. Li, X. Zhang, and X. Chen, "MOF-derived hierarchical carbon/ZnO hybrid synergistically boosts photothermal conversion and storage capability of phase change materials," Mater. Today Nano **20**, 100277 (2022).
[21]W. Ren, Y. Yan, L. Zeng, Z. Shi, A. Gong, P. Schaaf, D. Wang, J. Zhao, B. Zou, and H. Yu, "A near infrared light triggered hydrogenated black TiO_2 for cancer photothermal therapy," Adv. Healthcare Mater. **4**(10), 1526–1536 (2015).
[22]H. Wang, J. Shen, Y. Li, Z. Wei, G. Cao, Z. Gai, K. Hong, P. Banerjee, and S. Zhou, "Magnetic iron oxide–fluorescent carbon dots integrated nanoparticles for dual-modal imaging, near-infrared light-responsive drug carrier and photothermal therapy," Biomater. Sci. **2**(6), 915–923 (2014).
[23]Q. Wang, D. Niu, J. Shi, and L. Wang, "A three-in-one ZIFs-derived CuCo(O)/GOx@PCNs hybrid cascade nanozyme for immunotherapy/enhanced starvation/photothermal therapy," ACS Appl. Mater. Interfaces **13**(10), 11683–11695 (2021).
[24]M. S. Irshad, N. Arshad, and X. Wang, "Nanoenabled photothermal materials for clean water production," Global Challenges **5**(1), 2000055 (2021).
[25]Y. Zhao, Y. Meng, P. Yu, X. Hu, J. Su, and J. Han, "Modified reduced graphene oxide-LDH/WPU nanohybrid coated nylon 6 fabrics for durable photothermal conversion performance," Appl. Surf. Sci. **622**, 156900 (2023).
[26]Y. Hou, M. Gao, R. An, W. S. Tey, B. Li, J. Chen, L. Zhao, and K. Zhou, "Surface modification of oriented glass fibers for improving the mechanical properties and flame retardancy of polyamide 12 composites printed by powder bed fusion," Addit. Manuf. **62**, 103195 (2023).
[27]S. Sun, M. Brandt, and M. Easton, "Powder bed fusion processes: An overview," in *Laser Additive Manufacturing: Materials, Design, Technologies, and Applications* (Woodhead Publishing, 2017), pp. 55–77.
[28]J. Chen, L. Zhao, and K. Zhou, "Multi-jet fusion 3D voxel printing of conductive elastomers," Adv. Mater. **34**, 2205909 (2022).
[29]Z. Liu, Z. Zhou, N. Wu, R. Zhang, B. Zhu, H. Jin, Y. Zhang, M. Zhu, and Z. Chen, "Hierarchical photothermal fabrics with low evaporation enthalpy as heliotropic evaporators for efficient, continuous, salt-free desalination," ACS Nano **15**(8), 13007–13018 (2021).
[30]Y. Xia, Q. Hou, H. Jubaer, Y. Li, Y. Kang, S. Yuan, H. Liu, M. W. Woo, L. Zhang, and L. Gao, "Spatially isolating salt crystallisation from water evaporation for continuous solar steam generation and salt harvesting," Energy Environ. Sci. **12**(6), 1840–1847 (2019).
[31]M. Sheng, Y. Yang, X. Bin, S. Zhao, C. Pan, F. Nawaz, and W. Que, "Recent advanced self-propelling salt-blocking technologies for passive solar-driven interfacial evaporation desalination systems," Nano Energy **89**, 106468 (2021).
[32]J. Wang, Y. Kong, Z. Liu, and H. Wang, "Solar-driven interfacial evaporation: Design and application progress of structural evaporators and functional distillers," Nano Energy **108**, 108115 (2022).
[33]H. Liu, X. Zhang, Z. Hong, Z. Pu, Q. Yao, J. Shi, G. Yang, B. Mi, B. Yang, X. Liu *et al.*, "A bioinspired capillary-driven pump for solar vapor generation," Nano Energy **42**, 115–121 (2017).
[34]M. Zhu, Y. Li, F. Chen, X. Zhu, J. Dai, Y. Li, Z. Yang, X. Yan, J. Song, Y. Wang *et al.*, "Plasmonic wood for high-efficiency solar steam generation," Adv. Energy Mater. **8**(4), 1701028 (2018).
[35]A. Awad, F. Fina, A. Goyanes, S. Gaisford, and A. W. Basit, "Advances in powder bed fusion 3D printing in drug delivery and healthcare," Adv. Drug Delivery Rev. **174**, 406–424 (2021).
[36]S. Yuan, S. Li, J. Zhu, and Y. Tang, "Additive manufacturing of polymeric composites from material processing to structural design," Composites, Part B **219**, 108903 (2021).
[37]O. Diegel, A. Nordin, D. Motte, O. Diegel, A. Nordin, and D. Motte, *A Practical Guide to Design for Additive Manufacturing* (Springer, 2019), pp. 103–119.
[38]S. R. Churipard, K. S. Kanakikodi, D. A. Rambhia, C. S. K. Raju, A. Halgeri, N. V. Choudary, G. S. Ganesh, R. Ravishankar, and S. P. Maradur, "Porous polydivinylbenzene (PDVB) as an efficient adsorbent for hydrocarbons: Effect of porogens on adsorption capacity," Chem. Eng. J. **380**, 122481 (2020).
[39]N. Fechler, T. P. Fellinger, and M. Antonietti, ""Salt templating": A simple and sustainable pathway toward highly porous functional carbons from ionic liquids," Adv. Mater. **25**(1), 75–79 (2013).
[40]A. Pierre, M. Sadeghi, M. M. Payne, A. Facchetti, J. E. Anthony, and A. C. Arias, "All-printed flexible organic transistors enabled by surface tension-guided blade coating," Adv. Mater. **26**(32), 5722–5727 (2014).
[41]L. He, Y. Dong, Y. Zheng, Q. Jia, S. Shan, and Y. Zhang, "A novel magnetic MIL-101(Fe)/TiO_2 composite for photo degradation of tetracycline under solar light," J. Hazard. Mater. **361**, 85–94 (2019).
[42]W. Li, X. Wu, S. Li, W. Tang, and Y. Chen, "Magnetic porous Fe_3O_4/carbon octahedra derived from iron-based metal-organic framework as heterogeneous Fenton-like catalyst," Appl. Surf. Sci. **436**, 252–262 (2018).
[43]C. Li, Q. Hu, Y. Li, H. Zhou, Z. Lv, X. Yang, L. Liu, and H. Guo, "Hierarchical hollow Fe_2O_3@MIL-101(Fe)/C derived from metal-organic frameworks for superior sodium storage," Sci. Rep. **6**(1), 25556 (2016).
[44]Y. J. Tang, H. Zheng, Y. Wang, W. Zhang, and K. Zhou, "Laser-induced annealing of metal–organic frameworks on conductive substrates for electrochemical water splitting," Adv. Funct. Mater. **31**(31), 2102648 (2021).
[45]M. Qiao, X. Lei, Y. Ma, L. Tian, X. He, K. Su, and Q. Zhang, "Application of yolk–shell Fe_3O_4@N-doped carbon nanochains as highly effective microwave-absorption material," Nano Res. **11**, 1500–1519 (2018).
[46]J. Ding, L. Wang, Y. Zhao, L. Xing, X. Yu, G. Chen, J. Zhang, and R. Che, "Boosted interfacial polarization from multishell TiO_2@ Fe_3O_4@ PPy heterojunction for enhanced microwave absorption," Small **15**(36), 1902885 (2019).
[47]C. Yan, G. Chen, X. Zhou, J. Sun, and C. Lv, "Template-based engineering of carbon-doped Co_3O_4 hollow nanofibers as anode materials for lithium-ion batteries," Adv. Funct. Mater. **26**(9), 1428–1436 (2016).
[48]C. Cao, H. Zou, N. Yang, H. Li, Y. Cai, X. Song, J. Shao, P. Chen, X. Mou, W. Wang, and X. Dong, "Fe_3O_4/Ag/Bi_2MoO_6 photoactivatable nanozyme for self-replenishing and sustainable cascaded nanocatalytic cancer therapy," Adv. Mater. **33**(52), 2106996 (2021).
[49]C. Ding, Y. Zeng, L. Cao, L. Zhao, and Y. Zhang, "Hierarchically porous Fe_3O_4/C nanocomposite microspheres *via* a CO_2 bubble-templated hydrothermal approach as high-rate and high-capacity anode materials for lithium-ion batteries," J. Mater. Chem. A **4**(16), 5898–5908 (2016).
[50]H. Dong, W. Du, J. Dong, R. Che, F. Kong, W. Cheng, M. Ma, N. Gu, and Y. Zhang, "Depletable peroxidase-like activity of Fe_3O_4 nanozymes accompanied with separate migration of electrons and iron ions," Nat. Commun. **13**(1), 5365 (2022).
[51]G. Hu, J. Kang, L. W. T. Ng, X. Zhu, R. C. T. Howe, C. G. Jones, M. C. Hersam, and T. Hasan, "Functional inks and printing of two-dimensional materials," Chem. Soc. Rev. **47**(9), 3265–3300 (2018).

[52]B. Derby, "Inkjet printing of functional and structural materials: Fluid property requirements, feature stability, and resolution," Annu. Rev. Mater. Res. **40**, 395–414 (2010).
[53]F. Khazaie, S. Shokrollahzadeh, Y. Bide, S. Sheshmani, and A. S. Shahvelayati, "Forward osmosis using highly water dispersible sodium alginate sulfate coated-Fe_3O_4 nanoparticles as innovative draw solution for water desalination," Process Saf. Environ. Prot. **146**, 789–799 (2021).
[54]L. Su, J. Zhang, Y. Chen, W. Yang, J. Wang, Z. Ma, G. Shao, and G. Wang, "Cobalt-embedded hierarchically-porous hollow carbon microspheres as multi-functional confined reactors for high-loading Li-S batteries," Nano Energy **85**, 105981 (2021).
[55]Y. Hou, M. Gao, J. Chen, W. S. Tey, M. Chen, H. Zheng, B. Li, L. Zhao, and K. Zhou, "Preparation of iron oxide–coated aramid fibres for improving the mechanical performance and flame retardancy of multi-jet fusion–printed polyamide 12 composites," Virtual Phys. Prototyping **18**(1), e2171892 (2023).
[56]Y. Shi, O. Ilic, H. A. Atwater, and J. R. Greer, "All-day fresh water harvesting by microstructured hydrogel membranes," Nat. Commun. **12**(1), 2797 (2021).
[57]F. Wang, S. Zhao, X. Zhang, and Z. Su, "Interfacial solar evaporation based on Janus films: An effective strategy to improve salt tolerance and antifouling performance," Desalination **543**, 116085 (2022).
[58]A. M. Salhotra, E. E. Adams, and D. R. F. Harleman, "Effect of salinity and ionic composition on evaporation: Analysis of Dead Sea evaporation pans," Water Resour. Res. **21**(9), 1336–1344, https://doi.org/10.1029/WR021i009p01336 (1985).
[59]P. Mu, W. Bai, Y. Fan, Z. Zhang, H. Sun, Z. Zhu, W. Liang, and A. Li, "Conductive hollow kapok fiber-PPy monolithic aerogels with excellent mechanical robustness for efficient solar steam generation," J. Mater. Chem. A **7**(16), 9673–9679 (2019).
[60]Q. Chen, Z. Pei, Y. Xu, Z. Li, Y. Yang, Y. Wei, and Y. Ji, "A durable monolithic polymer foam for efficient solar steam generation," Chem. Sci. **9**(3), 623–628 (2018).
[61]S. Han, T. P. Ruoko, J. Gladisch, J. Erlandsson, L. Wågberg, X. Crispin, and S. Fabiano, "Cellulose-conducting polymer aerogels for efficient solar steam generation," Adv. Sustainable Syst. **4**(7), 2000004 (2020).
[62]J. He, G. Zhao, P. Mu, H. Wei, Y. Su, H. Sun, Z. Zhu, W. Liang, and A. Li, "Scalable fabrication of monolithic porous foam based on cross-linked aromatic polymers for efficient solar steam generation," Sol. Energy Mater. Sol. Cells **201**, 110111 (2019).
[63]J. He, Z. Zhang, C. Xiao, F. Liu, H. Sun, Z. Zhu, W. Liang, and A. Li, "High-performance salt-rejecting and cost-effective superhydrophilic porous monolithic polymer foam for solar steam generation," ACS Appl. Mater. Interfaces **12**(14), 16308–16318 (2020).
[64]S. Meng, T. Gong, X. Zhao, C.-Y. Tang, P. Yu, R.-Y. Bao, K. Ke, Z.-Y. Liu, M.-B. Yang, and W. Yang, "Boosting solar steam generation in dynamically tunable polymer porous architectures," Polymer **226**, 123811 (2021).
[65]P. Mu, W. Bai, Z. Zhang, J. He, H. Sun, Z. Zhu, W. Liang, and A. Li, "Robust aerogels based on conjugated microporous polymer nanotubes with exceptional mechanical strength for efficient solar steam generation," J. Mater. Chem. A **6**(37), 18183–18190 (2018).
[66]F. Liu, W. Liang, C. Wang, J. He, C. Xiao, Z. Zhu, H. Sun, and A. Li, "Superwetting monolithic hypercrosslinked polymers nanotubes with high salt-resistance for efficient solar steam generation," Sol. Energy Mater. Sol. Cells **221**, 110913 (2021).
[67]M. Tan, J. Wang, W. Song, J. Fang, and X. Zhang, "Self-floating hybrid hydrogels assembled with conducting polymer hollow spheres and silica aerogel microparticles for solar steam generation," J. Mater. Chem. A **7**(3), 1244–1251 (2019).
[68]Y. Jin, J. Chang, Y. Shi, L. Shi, S. Hong, and P. Wang, "A highly flexible and washable nonwoven photothermal cloth for efficient and practical solar steam generation," J. Mater. Chem. A **6**(17), 7942–7949 (2018).
[69]C. Li, D. Jiang, B. Huo, M. Ding, C. Huang, D. Jia, H. Li, C.-Y. Liu, and J. Liu, "Scalable and robust bilayer polymer foams for highly efficient and stable solar desalination," Nano Energy **60**, 841–849 (2019).
[70]J. Jia, W. Liang, H. Sun, Z. Zhu, C. Wang, and A. Li, "Fabrication of bilayered attapulgite for solar steam generation with high conversion efficiency," Chem. Eng. J. **361**, 999–1006 (2019).
[71]Z. Wang, M. Han, F. He, S. Peng, S. B. Darling, and Y. Li, "Versatile coating with multifunctional performance for solar steam generation," Nano Energy **74**, 104886 (2020).
[72]J. Yuan, X. Lei, C. Yi, H. Jiang, F. Liu, and G. J. Cheng, "3D-printed hierarchical porous cellulose/alginate/carbon black hydrogel for high-efficiency solar steam generation," Chem. Eng. J. **430**, 132765 (2022).